# Lawrence Berkeley National Laboratory

## LBL Publications

**Title**

DESI and DECaLS (D&amp;D): galaxy—galaxy lensing measurements with 1 per cent survey and its forecast

**Permalink**

https://escholarship.org/uc/item/1g1574dq

**Journal**

Monthly Notices of the Royal Astronomical Society, 524(4)

**ISSN**

**Authors**

Yao, Ji

Shan, Huanyuan

Zhang, Pengjie

et al.

**Publication Date**

2023-07-29

**DOI**

**Copyright Information**

Peer reviewed

# DESI and DECaLS (D&D): galaxy–galaxy lensing measurements with 1 per cent survey and its forecast

Ji Yao [1,2,3]★ Huanyuan Shan,[1,4]★ Pengjie Zhang,[2,3,5]★ Eric Jullo,[6] Jean-Paul Kneib,[6,7] Yu Yu [2,3] Ying Zu [2,3] David Brooks,[8] Axel de la Macorra,[9] Peter Doel,[8] Andreu Font-Ribera [10] Satya Gontcho A. Gontcho [11] Theodore Kisner,[11] Martin Landriau,[11] Aaron Meisner,[12] Ramon Miquel,[10,13] Jundan Nie,[14] Claire Poppett,[11,15,16] Francisco Prada,[17] Michael Schubnell,[18,19] Mariana Vargas Magana[9] and Zhimin Zhou[14]

[1] *Shanghai Astronomical Observatory (SHAO), Nandan Road 80, Shanghai 200030, China*
[2] *Department of Astronomy, School of Physics and Astronomy, Shanghai Jiao Tong University, Shanghai 200240, China*
[3] *Key Laboratory for Particle Astrophysics and Cosmology (MOE)/Shanghai Key Laboratory for Particle Physics and Cosmology, 200240, China*
[4] *University of Chinese Academy of Sciences, Beijing 100049, China*
[5] *Tsung-Dao Lee Institute, Shanghai Jiao Tong University, Shanghai 200240, China*
[6] *Aix-Marseille Univ, CNRS, CNES, LAM, Marseille 13013, France*
[7] *Institute of Physics, Laboratory of Astrophysics, Ecole Polytechnique Fédérale de Lausanne (EPFL), Observatoire de Sauverny, CH-1290 Versoix, Switzerland*
[8] *Department of Physics and Astronomy, University College London, Gower Street, London WC1E 6BT, UK*
[9] *Instituto de Física, Universidad Nacional Autónoma de México, CP 04510 Ciudad de México, Mexico*
[10] *Institut de Física d'Altes Energies (IFAE), The Barcelona Institute of Science and Technology, Campus UAB, E-08193 Bellaterra, Barcelona, Spain*
[11] *Lawrence Berkeley National Laboratory, 1 Cyclotron Road, Berkeley, CA 94720, USA*
[12] *NSF's NOIRLab, 950 N Cherry Ave, Tucson, AZ 85719, USA*
[13] *Institució Catalana de Recerca i Estudis Avançats, Passeig de Lluís Companys 23, E-08010 Barcelona, Spain*
[14] *National Astronomical Observatories, Chinese Academy of Sciences, A20 Datun Road, Chaoyang District, Beijing 100012, China*
[15] *Space Sciences Laboratory, University of California, Berkeley, 7 Gauss Way, Berkeley, CA 94720, USA*
[16] *University of California, Berkeley, 110 Sproul Hall #5800, Berkeley, CA 94720, USA*
[17] *Instituto de Astrofísica de Andalucía (CSIC), Glorieta de la Astronomía, s/n, E-18008 Granada, Spain*
[18] *Department of Physics, University of Michigan, Ann Arbor, MI 48109, USA*
[19] *University of Michigan, Ann Arbor, MI 48109, USA*

## ABSTRACT

The shear measurement from the Dark Energy Camera Legacy Survey (DECaLS) provides an excellent opportunity for galaxy–galaxy lensing study with the Dark Energy Spectroscopic Instrument (DESI) galaxies, given the large ($\sim$9000 deg$^2$) sky overlap. We explore this potential by combining the DESI 1 per cent survey and DECaLS Data Release 8 (DR8). With $\sim$106 deg$^2$ sky overlap, we achieve significant detection of galaxy–galaxy lensing for Bright Galaxy Survey (BGS) and luminous red galaxy (LRG) as lenses. Scaled to the full BGS sample, we expect the statistical errors to improve from 18(12) per cent to a promising level of 2(1.3) per cent at $\theta > 8$ arcmin ($< 8$ arcmin). This brings stronger requirements for future systematics control. To fully realize such potential, we need to control the residual multiplicative shear bias $|m| < 0.006$ and the bias in the mean redshift $|\Delta z| < 0.008$, requiring the introduced bias in the measurement is $<0.31\sigma$. We also expect significant detection of galaxy–galaxy lensing with DESI LRG/emission line galaxy (ELG) full samples as lenses, and cosmic magnification of ELG through cross-correlation with low-redshift DECaLS shear. If such systematical error control can be achieved, we find the advantages of DECaLS, comparing with the Kilo Degree Survey (KiDS) and the Hyper Suprime-Cam (HSC), are at low redshift, large scale, and in measuring the shear ratio (to $\sigma_R \sim 0.04$) and cosmic magnification.

**Key words:** gravitational lensing: weak – (cosmology:) large-scale structure of Universe – cosmology: observations.

## 1 INTRODUCTION

Weak gravitational lensing is one of the most promising cosmological probes in studying the nature of dark matter, dark energy, and gravity

(Refregier 2003; Mandelbaum 2018). The combination between different probes can be even more powerful, due to more constraining power and breaking the degeneracy between the parameters (Planck Collaboration I 2020; Abbott et al. 2022). However, possibly due to residual systematics or new physics beyond the standard $\Lambda$ cold dark matter ($\Lambda$CDM) model, the tension between cosmic microwave background (CMB) at redshift $z \sim 1100$ and the late-time galaxy surveys at $z < \sim 1$ troubles us when using their synergy

(Hildebrandt et al. 2017; Hikage et al. 2019; Hamana et al. 2020; Planck Collaboration I 2020; Asgari et al. 2021; Heymans et al. 2021; Abbott et al. 2022; Amon et al. 2022; Secco et al. 2022). Many attempts have been made to examine this tension, in terms of different systematics (Yao et al. 2017, 2020; Fong et al. 2019; Kannawadi et al. 2019; Pujol et al. 2020; Wright et al. 2020; Mead et al. 2021; Amon et al. 2022; Secco et al. 2022; Yamamoto et al. 2023), different statistics (Lin & Ishak 2017; Shan et al. 2018; Chang et al. 2019; Asgari et al. 2021; Harnois-Déraps et al. 2021; Joachimi et al. 2021; Leauthaud et al. 2022; Sánchez et al. 2022), and possible new physics (Jedamzik, Pogosian & Zhao 2021). We also refer to recent reviews for the readers' references (Mandelbaum 2018; Perivolaropoulos & Skara 2022).

To fully understand the physics behind this so-called 'S$_8$' tension, different cosmological probes are required, as their sensitivities to the systematics are different. Many new observations are also needed, to explore different redshift ranges, sky patches, and even equipment properties. Among the many proposed Stage IV galaxy surveys like Dark Energy Spectroscopic Instrument (DESI; DESI Collaboration et al. 2016a,b), Vera C. Rubin Observatory's Legacy Survey of Space and Time (LSST; LSST Science Collaboration et al. 2009), *Euclid* (Laureijs et al. 2011), *Roman Space Telescope* (or *WFIRST*; Spergel et al. 2015), and *China Space Station Telescope* (*CSST*; Gong et al. 2019), DESI is the only one currently operating and has measured more than 7.5 million redshifts so far.

DESI itself will provide tremendous constraining power in studying the expansion history of the Universe and the large-scale structure (DESI Collaboration et al. 2016a). Its cross-correlations with other lensing surveys (referred to as galaxy–galaxy lensing or g–g lensing) will provide not only more, but also independent cosmological information (Joudaki et al. 2018; Prat et al. 2022; Sánchez et al. 2022), while it can be used to study the galaxy–matter relation (Leauthaud et al. 2017, 2022), test gravity (Zhang et al. 2007; Jullo et al. 2019; Blake et al. 2020), and study the systematics (Zhang 2010; Zhang, Pen & Bernstein 2010; Yao et al. 2017, 2020; Giblin et al. 2021). However, Stage III surveys like Dark Energy Survey (DES; Abbott et al. 2022), Kilo-Degree Survey (KiDS; Heymans et al. 2021), and Hyper-Suprime Cam (HSC; Hikage et al. 2019) do not offer extremely large overlap with DESI, while the Stage IV surveys mentioned previously will require many years of observations before reaching their full overlap with DESI. In short, the sky overlap will limit the cross-correlation studies with DESI in the near future.

In this work, we study the cross-correlations between galaxy shear measured from the Dark Energy Camera Legacy Survey (DECaLS) Data Release 8 (DR8) and galaxies from the DESI 1 per cent (SV3) survey, and compare those with the overlapped data from KiDS and HSC. We measure the g–g lensing signals of the different weak lensing surveys with DESI 1 per cent survey and estimate their signal-to-noise ratio (S/N) that can be achieved with full DESI in the future. We explore the advantages of DECaLS, and exhibit the measurements of shear ratio and cosmic magnification as two promising tools in using the great constraining power of DECaLS×DESI. Additionally, to achieve the expected precision, we propose requirements on the DECaLS data, in terms of the shear calibration and the redshift distribution calibration.

This work is organized as follows. In Section 2, we briefly introduce the observables and their theoretical predictions. In Section 3, we describe the DESI, DECaLS, KiDS, and HSC data we use. In Section 4, we show the g–g lensing measurements for different DESI density tracers and different lensing surveys, and the measurements

of shear ratio and cosmic magnification. We summarize our findings from DESI×DECaLS for the 1 per cent survey in Section 5.

## 2 THEORY

In this section, we briefly review the theory of the g–g lensing observables. We assume spatial curvature $\Omega_k = 0$ so that the comoving radial distance equals the comoving angular diameter distance.

### 2.1 Galaxy–galaxy lensing

Since the foreground gravitational field distorts the shape of the background galaxy, there is a correlation between the background galaxies' gravitational shear $\gamma^G$ and the foreground galaxies' number density $\delta_g$. The correlation of $\langle \delta_g \gamma^G \rangle$ (or $w^{gG}$) will probe the clustering of the underlying matter field $\langle \delta_m \delta_m \rangle$ (or the matter power spectrum $P_\delta(k)$), the galaxy bias $b_g(k, z)$, and the redshift–distance relation, which are sensitive to the cosmological model and gravitational theory. We recall the g–g lensing angular power spectrum (Prat et al. 2022):

$$C^{g\kappa}(\ell) = \int_0^{\chi_{max}} \frac{n_l(\chi)q_s(\chi)}{\chi^2} b_g(k, z) P_\delta \left( k = \frac{\ell + 1/2}{\chi}, z \right) d\chi, \quad (1)$$

which is a weighted projection from the 3D non-linear matter power spectrum $P_\delta(k, z)$ to the 2D galaxy-lensing convergence angular power spectrum $C^{g\kappa}(\ell)$. It will also depend on the galaxy bias $b_g = \delta_g/\delta_m$, the comoving distance $\chi$, the redshift distribution of the lens galaxies $n_l(\chi) = n_l(z)dz/d\chi$, and the lensing efficiency as a function of the lens position (given the distribution of the source galaxies) $q_s(\chi)$, which is written as

$$q_s(\chi_l) = \frac{3}{2} \Omega_m \frac{H_0^2}{c^2} (1 + z_l) \int_{\chi_l}^\infty n_s(\chi_s) \frac{(\chi_s - \chi_l)\chi_l}{\chi_s} d\chi_s, \quad (2)$$

where $n_s(\chi_s)$ denotes the distribution of the source galaxies as a function of comoving distance, while $\chi_s$ and $\chi_l$ denote the comoving distance to the source and the lens, respectively.

The real-space galaxy–shear correlation function can be obtained through the Hankel transformation,

$$w^{gG}(\theta) = \frac{1}{2\pi} \int_0^\infty d\ell \ell C^{g\kappa}(\ell) J_2(\ell\theta), \quad (3)$$

where $J_2(x)$ is the Bessel function of the first kind with order 2. The 'G' represents the gravitational lensing shear $\gamma^G$, which is conventionally used to separate from the intrinsic alignment $\gamma^I$, whose contribution is ignored in this work due to the photo-$z$ separation shown later in Section 4. The Hankel transformation is calculated using FFTLOG.[1]

Therefore, by observing the correlation of $w^{gG}$, we can derive the constraints on the cosmological parameters through equation (1), $P_\delta(k)$ and $\chi(z)$. In order to get an accurate cosmology constraint, many systematics need to be considered, for example, the shear calibration error that can shift the measurement of $w^{gG}$, the inaccurate estimation of redshift distribution for the source $n_s(\chi_s(z_s))$ that can bias the theoretical prediction of equation (1), the massive neutrino effects and the baryonic effects that can bias the matter power spectrum $P_\delta(k, z)$, and the non-linear galaxy bias $b_g(k,$

---

[1] https://jila.colorado.edu/~ajsh/FFTLog/

$z$).[2] In this work, we mainly focus on the statistical significance for DESI×DECaLS, rather than the systematics. The theoretical calculation in this work are performed using the CCL(Chisari et al. 2019) package, with non-linear matter power spectrum calculated by HALOFIT (Takahashi et al. 2012). The fiducial cosmology in this work is KiDS-1000 Complete Orthogonal Sets of E/B-Integrals (COSEBI) ΛCDM cosmology with maximum a posteriori (MAP) of the full multivariate distribution (Asgari et al. 2021), which has $h = 0.727$, $\Omega_b h^2 = 0.023$, $\Omega_c h^2 = 0.105$, $n_s = 0.949$, and $\sigma_8 = 0.772$.

## 2.2 Shear ratio

The g–g lensing two-point statistics normally contain stronger detection significance at the small scale than at the large scale, due to a stronger gravitational lensing field (higher signal) and more independent angular modes (smaller statistical error). However, due to the inaccurate modelling of small-scale effects, such as the non-linear galaxy bias $b_g(k, z)$, suppression in the matter power spectrum $P_\delta(k)$ due to massive neutrino and baryonic effects, etc., the small-scale information is conventionally abandoned (Heymans et al. 2021; Abbott et al. 2022; Lee et al. 2022). However, by choosing the same lens galaxies with source galaxies at different redshifts, i.e. with the same redshift distribution $n_u(z)$ for the lens while different redshift distribution $n_v(z)$ and $n_w(z)$ for the sources, the ratio between the angular power spectra $C_{uv}^{g\kappa}$ and $C_{uw}^{g\kappa}$ (or the correlation functions $w_{uv}^{gG}$ and $w_{uw}^{gG}$) will mainly base on the two lensing efficiency functions as in equation (2) for the $v$th and $w$th source bins. This ratio does not suffer strongly from the modelling of the galaxy bias $b_g$ or the matter power spectrum $P_\delta(k)$, as they share the same lens sample according to equation (1). The shear ratio (or lensing ratio) has been used to improve cosmological constraints (Sánchez et al. 2022), as it is sensitive to the $\chi(z)$ relation in equation (2) and the nuisance parameters for the systematics, or to study the shear bias (Giblin et al. 2021). In this work, we will show the great potential of measuring shear ratio with DESI×DECaLS.

To account for the full covariance in measuring shear ratio $R = w_2/w_1$, and to prevent possible singular values when taking the ratio (when $w_1 \sim 0$), we construct the following data vector:

$$V = w_1 R - w_2,  \qquad (4)$$

which is designed to be 0 when $R$ is correctly predicted from the two data sets $w_1$ and $w_2$ that we want to take the ratio. The resulting covariance for the data vector $V$ is

$$C' = R^2 C_{11} + C_{22} - R(C_{12} + C_{21}),  \qquad (5)$$

where $C_{ij}$ is the covariance between $w_i$ and $w_j$. The likelihood of $-2\ln\mathscr{L} = V^T C'^{-1} V$ will give the posterior of the shear ratio $R$. To account for the covariance is $R$ dependent, normalization is done thereafter so that its probability density function (PDF) satisfies $\int P(R)\mathrm{d}R = 1$. An alternative way is to marginalize over the theoretical predictions $w_i$, similar to Dong et al. (2022) and Sun et al. (2023), which we leave for future studies.

---

[2]In this work, we use the mathematical classification of linear/non-linear bias as a matched filter, however, for more physical modelling, this is normally expressed as one-halo/two-halo terms and halo occupation distribution (HOD) descriptions such as central/satellite fractions (Leauthaud et al. 2017).

## 2.3 Cosmic magnification

The observed galaxy number density is affected by its foreground lensing signals, leading to an extra fluctuation besides the intrinsic clustering of galaxies, namely,

$$\delta_g^L = \delta_g + g_\mu \kappa,  \qquad (6)$$

where $\delta_g^L$ denotes the observed lensed galaxy overdensity, $\delta_g$ denotes the intrinsic overdensity of galaxies due to gravitational clustering, and $\kappa$ is the lensing convergence affecting the flux and the positions of the foreground galaxy sample, and due to the foreground inhomogeneities. For a complete and flux-limited sample, the magnification amplitude $g_\mu = 2(\alpha - 1)$. In that case, the magnification amplitude is sensitive to the galaxy flux function $N(F)$, denoting the number of galaxies brighter than flux limit $F$, with $\alpha = -\mathrm{d}\ln N/\mathrm{d}\ln F$.

According to equation (6), for a given galaxy sample at $z = z_1$, it not only contains clustering information of $\delta_g(z = z_1)$, but also has lensing information of $\kappa$ from the matter at $z < z_1$, which is normally treated as a contamination to the clustering signals (Deshpande & Kitching 2020; Kitanidis & White 2021; von Wietersheim-Kramsta et al. 2021). Meanwhile, attempts have been made to directly measure the cosmic magnification as a source of cosmological information (Yang et al. 2017; Gonzalez-Nuevo et al. 2021; Liu et al. 2021).

We follow the method of Liu et al. (2021) and correlate the shear galaxies at lower redshift (bin $i$) and the number density galaxies at higher redshift (bin $j$),

$$C_{ij}^{\kappa\mu}(\ell) = g_\mu \int_0^{\chi_{max}} \frac{q_i(\chi)q_j(\chi)}{\chi^2} P_\delta\left(k = \frac{\ell + 1/2}{\chi}, z\right) \mathrm{d}\chi,  \qquad (7)$$

which requires the redshift distribution of $n_i(z)$ being significantly separated from $n_j(z)$, so that the intrinsic clustering × lensing shear signal vanishes. The corresponding correlation function from the Hankel transformation is similar to equation (3).

## 2.4 Signal-to-noise ratio definition

The signal-to-noise ratio (S/N) definition in this work uses amplitude fitting. For a given measurement $w_{data}$ and an assumed theoretical model $w_{model}$, we fit an amplitude $A$ to the likelihood:

$$-2\ln\mathscr{L} = (w_{data} - Aw_{model})^T \mathrm{Cov}^{-1}(w_{data} - Aw_{model}),  \qquad (8)$$

so that a posterior of $A_{-\sigma_A}^{+\sigma_A}$ can be obtained, where $\sigma_A$ is the Gaussian standard deviation. Then the corresponding S/N is $A/\sigma_A$.

We note that, if $w_{data}$ is a single value rather than a data vector, this S/N defined by amplitude fitting is identical to the S/N of the data itself, namely $A/\sigma_A = w_{data}/\sigma_{w_{data}}$. This is the case for most of the S/N calculated in this work, when there is one single measurement at small scale and one at large scale, and the small-scale and large-scale data correspond to different (non-linear/linear) galaxy biases so they should be treated separately.

## 2.5 Systematics control

We follow Massey et al. (2013) and the treatments in Yao et al. (2023), and require the systematical error induced bias in the signal $\delta w_{sys}$ to satisfy

$$|\delta w_{sys}| \leq 0.31\sigma_w,  \qquad (9)$$

comparing with the statistical error $\sigma_w$ of the measurement. This requirement is only applied to the large-scale data of Bright Galaxy Survey (BGS), whose S/N is significantly larger than the other tracers, to decide the future calibration targets for DECaLS galaxy–galaxy lensing cosmology.

## 3 DATA

In this section, we introduce the DESI spectroscopic data and the shear catalogues from DECaLS/KiDS/HSC. We note even though the DES-Y3 catalogue is expected to have an overlap with full DESI for ∼1264 deg² , its overlap with DESI SV3 catalogue is 0. We, therefore, do not present any analysis for DES.

### 3.1 DESI

DESI is the only operating Stage IV galaxy survey. It is designed to cover 14 000 deg² of the sky, with 5000 fibres collecting spectra simultaneously (DESI Collaboration et al. 2016b; Silber et al. 2023; Miller et al. 2023). DESI aims to observe density tracers such as BGS (Ruiz-Macias et al. 2020), luminous red galaxies (LRGs; Zhou et al. 2020), emission line galaxies (ELGs; Raichoor et al. 2020), and quasi-stellar objects (QSOs; Yèche et al. 2020), with generally increasing redshift. Other supporting papers on target selections and validations can be find in Allende Prieto et al. (2020), Alexander et al. (2023), Chaussidon et al. (2023), Cooper et al. (2023), Hahn et al. (2023), Lan et al. (2023), and Zhou et al. (2023). DESI plans to use these tracers to study cosmology, especially in baryonic acoustic oscillations (BAO) and redshift-space distortions (RSDs; Levi et al. 2013; DESI Collaboration et al. 2016a). It is located on the 4-m Mayall Telescope in Kitt Peak, Arizona (DESI Collaboration et al. 2022). From 2021 till now, DESI has finished its 'SV3' (DESI Collaboration 2023a) and 'DA0.2' catalogues, which will be included in the coming Early Data Release (EDR; DESI Collaboration 2023b). The Siena Galaxy Atlas (Moustakas et al. 2023) is also expected soon.

The DESI experiment is based on the DESI Legacy Imaging Surveys (Zou et al. 2017; Dey et al. 2019; Schlegel et al. 2023), with multiple supporting pipelines in spectroscopic reduction (Guy et al. 2023), derivation of classifications and redshifts (Bailey et al.2023), fibre assignment (Raichoor et al.2023), survey optimization (Schlafly et al. 2023), and spectroscopic target selection (Myers et al. 2023)

In this work, we use the DESI SV3 catalogue, which is also known as the 1 per cent survey (with a sky coverage of ∼140 deg²), for the g–g lensing study. We consider the DESI BGS, LRGs, and ELGs, while ignoring the QSOs as the available number is relatively low. In SV3, each galaxy is assigned a weight to account for the survey completeness and redshift failure. Since the purpose of this paper is not a precise measurement of cosmology, we assume the linear galaxy biases follow $b_{BGS}(z)D(z) = 1.34$, $b_{LRG}(z)D(z) = 1.7$, and $b_{ELG}(z)D(z) = 0.84$, where $D(z)$ is the linear growth factor normalized to $D(z = 0) = 1$ (DESI Collaboration et al. 2016a). The number of galaxies used will be informed later in the paper, as the overlap between the DESI 1 per cent survey and the lensing surveys is different.

### 3.2 DECaLS

We use lensing shear measurement from DECaLS DR8, which contains galaxy images in $g$, $r$, and $z$ bands (Dey et al. 2019). DECaLS DR8 galaxies are processed by TRACTOR (Lang, Hogg & Schlegel 2016; Meisner, Lang & Schlegel 2017) and divided into five types according to their morphologies: PSF, SIMP, DEV, EXP, and COMP (Phriksee et al. 2020; Yao et al. 2020; Xu et al. 2021; Zu et al. 2021). The galaxy ellipticities $e_{1,2}$ are measured – except for the PSF type – with a joint fit on the $g$, $r$, and $z$ bands. A conventional shear calibration (Heymans et al. 2012; Miller et al. 2013; Hildebrandt et al. 2017) is applied as in

$$\gamma^{obs} = (1 + m)\gamma^{true} + c, \qquad (10)$$

with a multiplicative bias $m$ and additive bias $c$, to account for possible residual bias from PSF modelling, measurement method, blending, and crowding (Mandelbaum et al. 2015; Euclid Collaboration et al. 2019). This calibration is obtained by comparing with Canada–France–Hawaii Telescope (CFHT) Stripe-82 observed galaxies and OBIWAN simulated galaxies (Kong et al. 2020; Phriksee et al. 2020).

Several versions of the photometric redshift for the DECaLS galaxies have been estimated (Zou et al. 2019; Zhou et al. 2021; Duncan 2022). We apply the most widely used one (Zhou et al. 2021), which uses the $g$, $r$, and $z$ optical bands from DECaLS while borrowing $W1$ and $W2$ infrared bands from the *Wide-field Infrared Survey Explorer* (*WISE*; Wright et al. 2010). The photo-$z$ algorithm is trained based on a decision tree, with training samples constructed from a wide selection of spectroscopic redshift surveys and deep photo-$z$ surveys. We additionally require $z$-band magnitude $m_z < 21$ to select galaxies with better photo-$z$. We use the photo-$z$ distribution to represent the true-$z$ distribution $n(z)$, while allowing a systematic bias of $\Delta z$ in the form $n(z - \Delta z)$, to pass its effect to equation (2) then equation (1). This is appropriate as weak lensing is mainly biased due to the mean redshift but slightly affected by the redshift scatter.

Overall, the DR8 shear catalogue has ∼9000 deg² sky coverage – which will be the final overlap with full DESI – with an average galaxy number density of ∼1.9 galaxies arcmin⁻². The overlapped area with DESI 1 per cent survey is ∼106 deg², which is significantly larger than the other Stage III lensing surveys.

We note that the current DECaLS DR8 shear catalogue can have some residual multiplicative bias $|m| \sim 0.05$ (Phriksee et al. 2020; Yao et al. 2020), possibly due to the selections in observational data while making the comparison (Jarvis et al. 2016; Li et al. 2021) or due to source detection (Sheldon et al. 2020; Li & Mandelbaum 2023). This will prevent us from getting reliable cosmology for measurements with S/N > ∼20. Also, there exists a possible bias in the redshift distribution $n(z)$, which will require a galaxy colour-based algorithm (Hildebrandt et al. 2017; Buchs et al. 2019; Wright et al. 2020) or a galaxy clustering-based algorithm (Zhang et al. 2010; van den Busch et al. 2020; Peng et al. 2022) to get the correction. For these two reasons, we choose not to extend this study to the precision cosmology level. A future version of the DECaLS DR9 shear catalogue is under development, with improved data reduction and survey procedures,[3] with more advanced shear calibration for a pure OBIWAN image simulation-based algorithm (Yao et al. in preparation) and redshift calibration (Xu et al. in preparation).

### 3.3 KiDS

The Kilo-Degree Survey (KiDS) is run by the European Southern Observatory and is designed for weak lensing studies in *ugri* optical bands. The KiDS data are processed by THELI (Erben et al. 2013) and ASTRO-WISE (Begeman et al. 2013; de Jong et al. 2015). The galaxy shear measurements are obtained by LENSFIT (Miller et al. 2013; Fenech Conti et al. 2017), and the photo-$z$s are measured by BPZ (Benitez 2000; Benítez et al. 2004) using the KiDS *ugri* optical bands and the *ZYJHK$_s$* infrared bands from VIKING (Wright et al. 2019). The KiDS shears are calibrated following the same equation as equation (10) with image simulation (Kannawadi et al. 2019).

We use the KiDS-1000 shear catalogue (Asgari et al. 2021; Giblin et al. 2021) in this work. The overlapped area with DESI SV3 is

---

[3]https://www.legacysurvey.org/dr9/description/

$\sim$55 deg$^2$. The expected overlapped area between the full DESI footprint and KiDS-1000 is $\sim$456 deg$^2$.

## 3.4 HSC

The Hyper Suprime-Cam Subaru Strategic Program (HSC-SSP, or HSC) is a Japanese lensing survey using the powerful Subaru Telescope. It covers five photometric bands *grizy*. Compared with KiDS and DES, HSC has its unique advantage in the galaxy number density and high-$z$ galaxies (but with a smaller footprint). The HSC shears are calibrated similarly to equation (10) (Mandelbaum et al. 2018) but with an additional shear responsivity (Hamana et al. 2020).

We use the HSC-Y1 shear catalogue (Mandelbaum et al. 2018; Hikage et al. 2019; Hamana et al. 2020), which overlaps with DESI SV3 for $\sim$48 deg$^2$. The expected overlap between HSC-Y3 data and full DESI is $\sim$733 deg$^2$. We note this overlap is calculated from the HSC third data release (Aihara et al. 2022) but not the shape catalogue (Li et al. 2022a), which applies a minimum cut on the number of input exposures in five bands. We use the EPHOR AB photo-$z$ best fit for the HSC galaxies (Tanaka et al. 2018).

## 4 RESULTS

In this section, we show the measurements of different galaxy–shear correlation functions. The estimator for the galaxy–shear correlation is

$$w^{gG}(\theta) = \frac{\sum_{ED} w_E \gamma_E^+ w_D}{\sum_{ER}(1 + m_E) w_E w_R} - \frac{\sum_{ER} w_E \gamma_E^+ w_R}{\sum_{ER}(1 + m_E) w_E w_R}, \quad (11)$$

where $w_E$, $m_E$, and $\gamma_E^+$ denote the lensing weight (inverse-variance weight for DECaLS, Phriksee et al. 2020, and HSC, Hikage et al. 2019, an adjusted version for KiDS, Miller et al. 2013), the multiplicative bias correction (for HSC there is an extra shear responsivity included), and the tangential shear of the source galaxy, with respect to the given lens galaxy with weight $w_D$ or $w_R$. The $\Sigma$-summations are calculated for all the ellipticity–density (ED) pairs and the ellipticity–random (ER) pairs. We note equation (11) already includes the correction for boost factor (Mandelbaum et al. 2005; Amon et al. 2018), and this equation is adequate for the multiplicative bias $m_E$ defined either per galaxy or per sample. The correlation uses DESI official random catalogues to simultaneously correct for the additive bias in the presence of a mask and reduce the shape noise. We will show the measurements with different lens samples and source catalogues using the above estimator.

### 4.1 DESI $w^{gG}$

We first show the g–g lensing measurements for DESI BGS and the three shear catalogues. The normalized redshift distributions $n(z)$ are shown in Fig. 1, with the number of galaxies being used in the labels. We use BGS with $0 < z < 0.5$, and require the photo-$z$ of the source galaxies located at $0.6 < z_p < 1.5$, so that the overlap in redshift is very small even considering the inaccuracy of photo-$z$. We see that DECaLS has the most available BGS lenses, while HSC has the most available sources and the highest redshift. We notice there are unexpected spikes for the photo-$z$ distribution of KiDS, which is probably due to cosmic variance as the overlapped area is much smaller than the full KiDS data.

We show the measured correlation functions for the DESI BGS g–g lensing in Fig. 2. The correlations are measured in two logarithmic bins in $0.5 < \theta < 80$ arcmin, with the statistical uncertainties calculated using jackknife resampling. We find that all three lensing
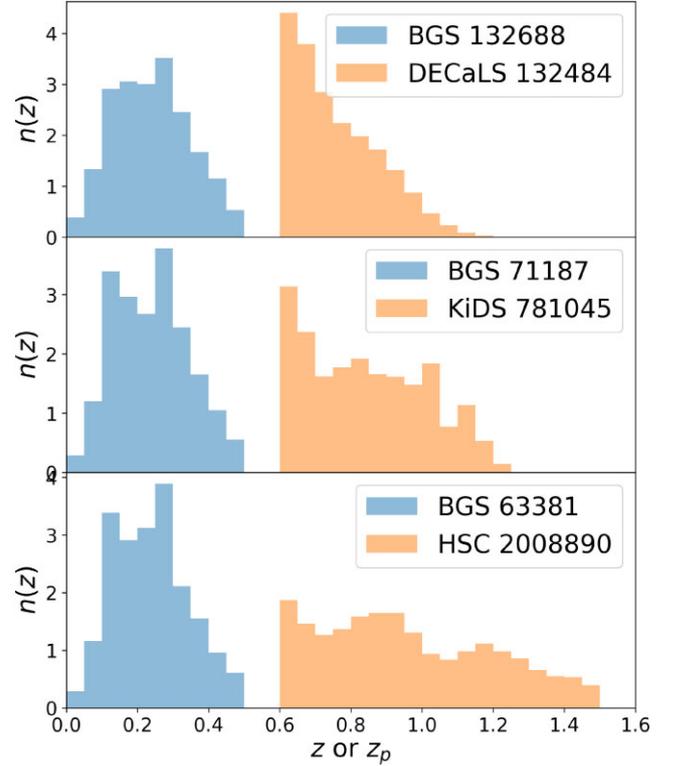


**Figure 1.** The galaxy redshift distributions for the DESI BGS with $0 < z < 0.5$ and photo-$z$ (point estimates) distributions for the lensing surveys with $0.6 < z_p < 1.5$. The numbers in the labels are the number of galaxies in the overlapped region.
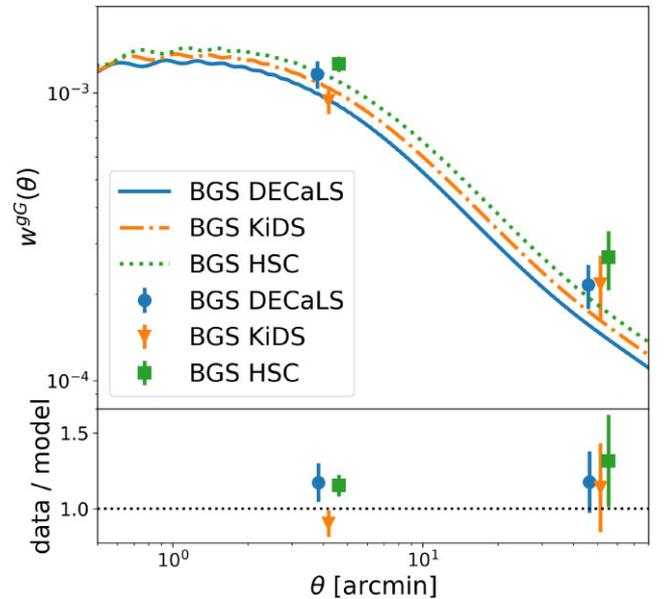


**Figure 2.** The galaxy–galaxy lensing angular correlation functions, corresponding to the galaxies samples in Fig. 1. In the upper panel, the theoretical curves are given by the fiducial cosmology and the assumed galaxy bias model. The (small-scale, large-scale) detection significances are (9.1, 5.8) for BGS×DECaLS, (10.2, 3.9) for BGS×KiDS, and (16.1, 4.3) for BGS×HSC. In the lower panel, we show the ratio between our measurements and the corresponding theoretical model, with the latter reweighted using the number of pairs and lensing weights to account for the band power problem with wide angular bins. The DECaLS and HSC results are slightly shifted horizontally.

surveys have strong g–g lensing signals, even for the current 1 per cent DESI data. The measurements are shown in blue dots (DECaLS), orange triangles (KiDS), and green squares (HSC), while the corresponding theoretical comparisons are shown in the blue solid curve, the orange dash–dotted curve, and the green dotted curve. From this figure, we find that the advantage of DECaLS is its large-scale cosmological information, with the highest S/N $\sim$ 5.8. This is due to DECaLS's significantly large overlap with DESI, reducing the cosmic variance. On the other hand, KiDS and HSC have larger S/N than DECaLS at small scale, due to their higher source galaxy number density, which lowers the shape noise.

In this work, we choose not to estimate the best-fitting cosmology, as for DECaLS, there are some unaddressed potential systematics (as discussed in Section 3.2), while for KiDS and HSC we do not want to harm the ongoing blinding efforts in the DESI Collaboration (although for a larger catalogue with the larger overlapped area). The theoretical estimations in Fig. 2 and all the other similar figures in this work are based on the KiDS-1000 COSEBI $\Lambda$CDM cosmology with MAP of the full multivariate distribution (Asgari et al. 2021), which has $h = 0.727$, $\Omega_b h^2 = 0.023$, $\Omega_c h^2 = 0.105$, $n_s = 0.949$, and $\sigma_8 = 0.772$. We note the choice of other fiducial cosmology (Hamana et al. 2020; Planck Collaboration I 2020; Asgari et al. 2021; Abbott et al. 2022) will give similar results for the current stage with DESI SV3. The linear galaxy biases are assumed following the descriptions of difference density tracers in Section 3.1.

We note that the choice of two log-bins is limited by the 20 jackknife subregions (Mandelbaum et al. 2006; Yao et al. 2020), which is limited by (1) the requirement of each jackknife subregion is independent up to the largest scale we use (80 arcmin), and (2) the size of the overlapped region for KiDS and HSC ($\sim$50 deg$^2$). As the DESI survey expands, the available overlapped region will increase accordingly, resulting in increase in both the available number of subregions and the maximum angular scale we can measure. Alternatively, we can use an analytical covariance (similar to Appendix A but more tests need to be done) or simulation-based covariance for future DESI data. We also note in this work the inverses of the covariances are corrected (Hartlap, Simon & Schneider 2007; Wang et al. 2020) due to the limited number of subregions.

As a demonstration of more angular binning, we use BGS×DECaLS data to show the choice of 50 jackknife subregions and five angular bins, as in Fig. 3. We show that with proper binning, more cosmological information can be extracted. The $\theta > \sim$2 arcmin measurements (the right four large-scale dots) agree with the linear bias assumption very well. In the future, with a larger overlapped footprint, more jackknife subregions can be used, so that more angular bins can be measured, either to increase the total S/N or to address any scale-dependent systematics. We do see great potential for DECaLS from the above results, although measurements will ultimately be limited by systematic errors.

We show the redshift distribution of the DESI LRGs and the three lensing surveys in Fig. 4, requiring $z < 0.6$ for the spec-$z$ LRGs and $0.7 < z_p < 1.5$ for the source galaxies. Similar to the BGS, more LRGs can be used when overlapping with DECaLS, while the available DECaLS source galaxies are less than in the other surveys. Since LRGs are generally distributed at higher $z$ than the BGS, we choose to increase the $z$-cut of the LRGs and the $z_p$-cut of the sources, resulting in reduced source galaxies compared with Fig. 1. This figure shows the DECaLS source galaxies are more reduced (from 133 000 to 78 000) as it is shallower than the other two.

The correlation measurements for the LRGs are presented in Fig. 5. At large scale, the DECaLS signal is weaker than KiDS and HSC, but
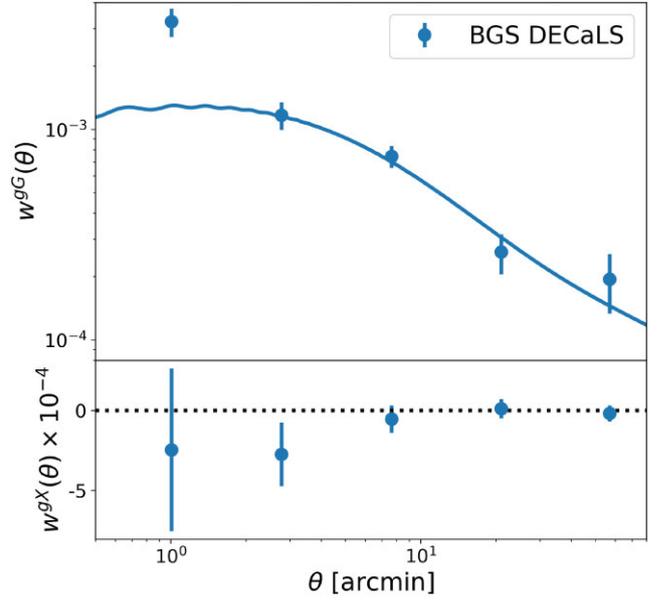
**Figure 3.** The galaxy–galaxy lensing angular correlation function $w^{gG}$ (upper panel) and its 45° rotation test $w^{gX}$ (lower panel) for the BGS×DECaLS g–g lensing only, with the same distribution as in Fig. 1 but with more angular bins with 50 jackknife subregions. In the upper panel, the theoretical curves are given by the fiducial cosmology and the assumed galaxy bias model. The detection significance for the five angular bins are (6.5, 6.6, 8.4, 4.7, 3.2), with the four large-scale bins well agreed with the prediction from fiducial cosmology and the linear bias assumption. The smallest scale measurement deviates from the theoretical prediction, demonstrating the breakdown of the linear galaxy bias assumption. The total S/N using amplitude fitting (as described in Section 2.4) is $8.9\sigma$ ($A = 1.03^{+0.12}_{-0.11}$) for the right three large-scale dots, and is $10.0\sigma$ ($A = 1.0^{+0.1}_{-0.1}$) for the right four large-scale dots. In the lower panel, where the shear are rotated for 45°, the results are consistent with 0, with reduced $\chi^2 \sim 3/5$.
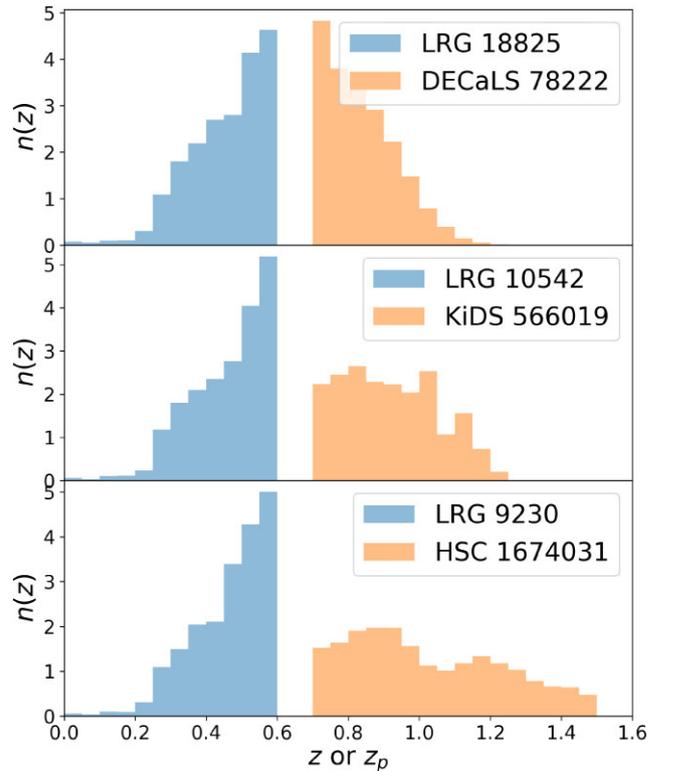


**Figure 4.** The galaxy redshift distributions for the DESI LRGs with $0 < z < 0.6$ and photo-$z$ distributions for the lensing surveys with $0.7 < z_p < 1.5$. The numbers in the labels are the number of galaxies in the overlapped region.
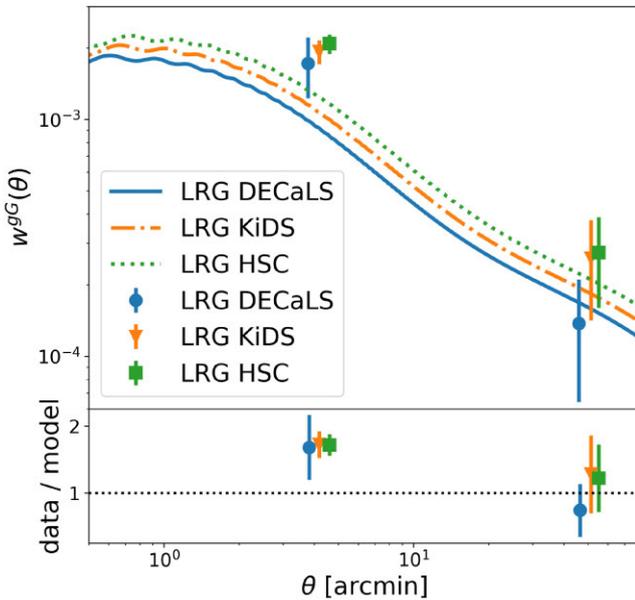
**Figure 5.** The galaxy–galaxy lensing angular correlation functions, corresponding to the galaxies samples in Fig. 4. In the upper panel, the theoretical curves are given by the fiducial cosmology and the assumed galaxy bias model. The (small scale, large scale) detection significances are (3.5, 1.9) for LRG×DECaLS, (8.7, 2.2) for LRG×KiDS, and (10.6, 2.4) for LRG×HSC.

it still offers comparable S/N. At the small scale, the S/N is dominated by deep surveys. The small-scale measurements are significantly higher than the theoretical predictions, due to LRGs being generally more massive than BGS, with stronger non-linear galaxy bias at such separations.

Furthermore, we study the g–g lensing measurements of the DESI ELGs. We show the redshift distribution of the DESI ELGs and the three lensing surveys in Fig. 6, requiring $z < 0.7$ for the spec-$z$ ELGs and $0.8 < z_{\rm p} < 1.5$ for the source galaxies. The available number of galaxies is further reduced compared to BGS and LRGs, due to DESI ELGs being mainly distributed at $z > 0.7$. And the high-$z$ sources for DECaLS are significantly less than KiDS and HSC.

The correlation measurements of the ELGs are shown in Fig. 7. HSC appears to have the largest S/N at both large scale and small scale, and the S/N of DECaLS at large scale is comparable to KiDS. All three lensing surveys have small-scale measurements lower than the theoretical predictions, suggesting the low measurement is not a systematics of DECaLS. We suspect this might be due to shape noise, sample variance, or possibly non-linear galaxy bias. As when we go from large scale to small scale, the non-linear halo bias for less massive haloes (e.g. the host haloes for ELGs, see Fig. 7) tends to drop compared with its linear bias, while the non-linear halo bias tends to increase for the more massive haloes (e.g. the host haloes for the LRGs, see Fig. 5) according to fig. 1 of Fong & Han (2021). The satellite galaxy fraction in the ELGs could also lead to a low amplitude at small scale (Favole et al. 2016; Niemiec et al. 2017; Gao et al. 2022). These will require a higher S/N to test in the future. In this work, we only focus on large-scale ELGs measurement.

### 4.2 Forecasts and systematics

We summarize our findings for the g–g lensing measurements from BGS (Fig. 2), LRGs (Fig. 5), and ELGs (Fig. 7) in Table 1. We see that DECaLS has its unique advantage in extracting cosmological information at large scale and at lower redshift (when correlating with
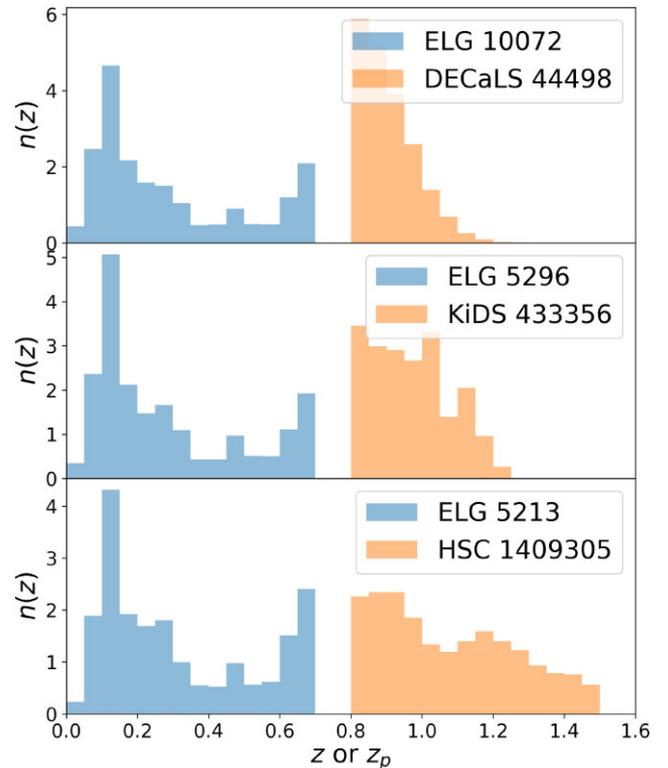


**Figure 6.** The galaxy redshift distributions for the DESI ELGs with $0 < z < 0.7$ and photo-$z$ distributions for the lensing surveys with $0.8 < z_{\rm p} < 1.5$. The numbers in the labels are the number of galaxies in the overlapped region.

the DESI BGS). Neglecting systematic errors for the moment, which will be dominant in practice, we give the forecast of the S/N with the complete DESI survey by rescaling the covariance according to the overlapped area. This rescaling assumes the covariance of the g–g lensing signal is dominated by the Gaussian covariance. Since we are extrapolating from small regions with significant boundary effects in our large-scale bin, this is only an approximation. We theoretically test the different components of the covariance in Appendix A for your interest. The large-scale information of future DECaLS×BGS can reach $>50\sigma$, which is stronger than most of the current g–g lensing data, and will be very promising in studying the current $S_8$ tension (Hildebrandt et al. 2017; Hikage et al. 2019; Hamana et al. 2020; Planck Collaboration I 2020; Asgari et al. 2021; Heymans et al. 2021; Abbott et al. 2022; Amon et al. 2022; Secco et al. 2022). The contribution from LRGs and ELGs, and possibly QSOs in the future, can also offer independent cosmological information.

We note that the S/N predictions in Table 1 ignored the potential bias from systematics, such as residual shear multiplicative bias $m$ and redshift distribution $n(z)$. The existence of the shear multiplicative bias $m$ will change the lensing efficiency from $q_{\rm s}$ to $(1 + m)q_{\rm s}$ in equations (1) and (2). The bias in redshift distribution $\Delta z$ will change the redshift distribution for the source galaxies from $n_{\rm s}(\chi_{\rm s}(z_{\rm s}))$ to $n_{\rm s}(\chi_{\rm s}(z_{\rm s} - \Delta z))$ in equation (2), so that the whole redshift distribution is shifted towards higher $z$ direction by $\Delta z$. For example, if we assume the residual multiplicative bias is $|m| \sim 0.05$ (which is found for some DECaLS galaxy subsamples as in Phriksee et al. 2020; Yao et al. 2020), and enlarge the covariance to account for this potential bias, then the S/N of DECaLS×BGS at large scale will be reduced from $>50\sigma$ to $\sim20\sigma$. This is a huge loss of cosmological information, although $\sim20\sigma$ is still comparable
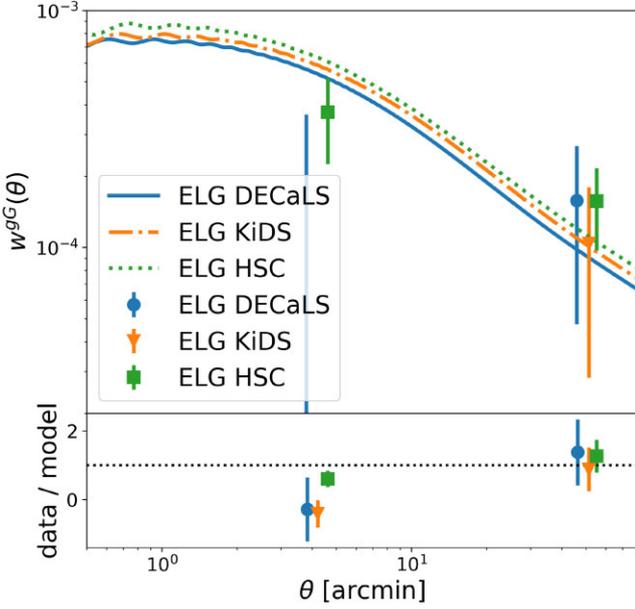
**Figure 7.** The galaxy–galaxy lensing angular correlation functions, corresponding to the galaxies samples in Fig. 6. The theoretical curves are given by the fiducial cosmology and the assumed galaxy bias model. The (small scale, large scale) detection significance are $(-0.3, 1.4)$ for ELG×DECaLS, $(-1.1, 1.4)$ for ELG×KiDS, and $(2.5, 2.6)$ for ELG×HSC. The negative values at small scale represent negative measurements, which might be due to the non-linear galaxy bias, satellite fraction, or shot noise.

to the $\sim 11\sigma$ of KiDS-DR4 and $\sim 17\sigma$ of HSC-Y3. Therefore, we emphasize the importance of calibrating DECaLS data in a more precise way in the future for reliable cosmological measurements. We note the current measurements with DESI 1 per cent survey have S/N $\ll 20\sigma$, therefore the impacts from such biases are still within the error budget. The assumed systematics can enlarge the large(small-scale) uncertainties from $\sim 17$ per cent ($\sim 10$ per cent) to $\sim 18$ per cent ($\sim 12$ per cent).

We further estimate the requirements on the DECaLS calibrations for precision cosmology. We evaluate the fractional bias in the measured correlation function $w^{\mathrm{gG}}$, considering some residual multiplicative bias $m$ and redshift bias $\Delta z$, and present the results in Fig. 8. To safely use the $\sim 50\sigma$ data from the large scale of DECaLS×BGS, the residual multiplicative bias alone need to be controlled within $|m| < 0.02$, and the mean of the redshift distribution of the source galaxies $\langle z \rangle$ need to be controlled within $|\Delta z| < 0.03$ on its own. The net bias considering both $m$ and $\Delta z$ should be controlled in between the orange dotted curves in Fig. 8. To safely use the cosmological information in both the large scale and the small scale, with overall S/N $\sim 100\sigma$, we require the calibrations to have $|m| < 0.01$ and $|\Delta z| < 0.015$ individually, while the net bias considering both $m$ and $\Delta z$ should be controlled in between the blue dashed curves in Fig. 8.

We note that using tomography and combining g–g lensing measurements from different density tracers (BGS, LRGs, ELGs, and possibly QSOs in the future) can bring stronger S/N, so the requirements on the calibration terms will be stricter. However, these studies will require a much larger covariance, thus more jackknife subregions and much larger overlapped regions, which are beyond

**Table 1.** Forecast the future statistical power (upper table) and calibration targets for the systematics (lower table) for DESI g–g lensing. We summarize the S/N of the DESI 1 per cent survey (SV3) g–g lensing results in Figs 2, 5, and 7, and forecast the ideal final S/N with full DESI, by rescaling the covariance based on the overlapped area, assuming DECaLS data can be well calibrated. We note that the ELG measurements become negative sometimes, and therefore decide not to predict its final S/N. From this table, we see that the advantage of DECaLS is at low-$z$ (with BGS) and large scale. In the lower part of the table, we focus on the forecast for the large-scale results (for cosmology) with DESI BGS (as they have the highest S/N), and additionally present the possible bias in the forecasted S/N, namely $\Delta$S/N. It includes the contribution from the statistical error of the current measurement, and residual systematical bias from the data calibration. The statistical contribution of $\Delta$S/N results from rescaling the $1\sigma$ error from Figs 2, 5, and 7, and is scale independent and redshift independent. The contribution from multiplicative bias $m$ is also scale independent, while the contribution from redshift bias $\Delta z$ is weakly scale dependent and redshift dependent. We use multiplicative bias $|m| \sim 0.05$ (Phriksee et al. 2020; Yao et al. 2020) and redshift bias $|\Delta z| \sim 0.02$ (Zhou et al. 2021) for DECaLS DR8, $|m| \leq 0.015$ and $|\Delta z| \leq 0.013$ for KiDS (Asgari et al. 2021), and $|m| \sim 0.01$ and $|\Delta z| \leq 0.038$ for HSC (Hikage et al. 2019; Li et al. 2023) to predict their systematical error in the forecasted S/N. We also estimate the tolerance for the biases using the requirement of $<0.31\sigma$ following Section 2.5. If the potential bias is smaller than the tolerance, we suggest the calibration target is satisfied already.

| Survey | SV3 overlap (deg$^2$) | SV3 S/N [small scale, large scale] | | | Full overlap (deg$^2$) | Ideal forecast S/N [small scale, large scale] | | |
|---|---|---|---|---|---|---|---|---|
| | | BGS | LRG | ELG | | BGS | LRG | ELG |
| DECaLS | 106 | [9.1, 5.8] | [3.5, 1.9] | [−0.3, 1.4] | ∼9000 | [83.8, 53.4] | [32.2, 17.5] | [N/A, 12.9] |
| KiDS | 55 | [10.2, 3.9] | [8.7, 2.2] | [−1.1, 1.4] | 456 (DR4) | [29.3, 11.2] | [25.1, 6.3] | [N/A, 4.0] |
| HSC | 48 | [16.1, 4.3] | [10.6, 2.4] | [2.5, 2.6] | 733 (Y3) | [62.9, 16.8] | [41.4, 9.4] | [9.8, 10.2] |

| Survey (×BGS, large scale) | Forecast potential bias $\Delta$S/N | | Bias tolerance | | Calibration satisfied? (Y/N) | |
|---|---|---|---|---|---|---|
| | Statistical | Systematical | $m$ | $\Delta z$ | $m$ | $\Delta z$ |
| DECaLS | ±9.2 | ±5 per cent ($m$) ± 1.4 per cent ($\Delta z$) | 0.006 | 0.008 | N | N |
| KiDS | ±2.9 | ±1.5 per cent ($m$) ± 0.8 per cent ($\Delta z$) | 0.028 | 0.045 | Y | Y |
| HSC | ±3.9 | ±1 per cent ($m$) ± 1.6 per cent ($\Delta z$) | 0.018 | 0.043 | Y | Y |

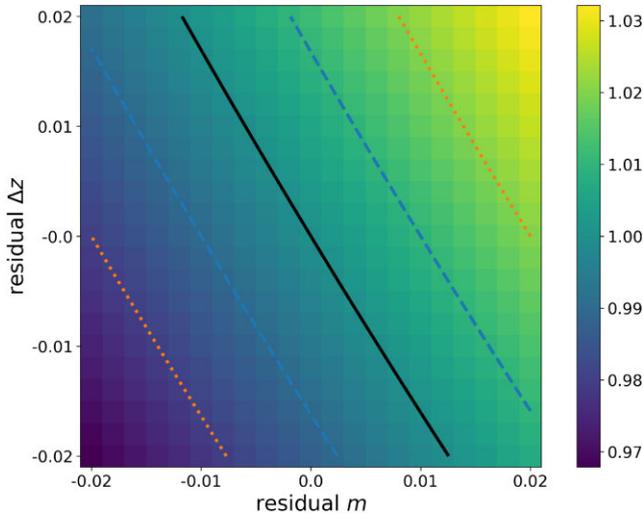**Figure 8.** The impact of the residual shear multiplicative bias $m$ and the bias in the redshift distribution $\Delta z$. For different $m$ and $\Delta z$, we evaluate the resulting $w_{\rm bias}/w_{\rm true}$ at the large scale of Figs 2, 5, and 7 ($\theta \sim 51$ arcmin) and show the ratio as the colour map. The effect of $m$ is totally scale independent, while the effect of $\Delta z$ is weakly scale dependent, which can bring an additional $\sim 20$ per cent difference at maximum. We also show where the bias from $m$ and $\Delta z$ perfectly cancel each other (black solid curve), and the location where the net bias reaches $\pm 0.01$ (blue dashed curve) and $\pm 0.02$ (orange dotted curve).

the ability of the current data size. We leave this study to future works.

### 4.3 Shear ratio

Shear ratio is a powerful tool to probe cosmology or test systematics (Giblin et al. 2021; Sánchez et al. 2022), and it is insensitive to many small-scale physics. As shown in Table 1, DECaLS×DESI, especially for the BGS and LRGs, can offer very high S/N measurements at the small scale. We take the BGS from the DESI 1 per cent survey as an example to study this topic.

The galaxy samples are distributed similarly to the BGS×DECaLS $n(z)$ as in Fig. 1, but in addition, the source galaxies are further split into two groups: $0.6 < z_{\rm p} < 0.9$ and $0.9 < z_{\rm p} < 1.5$. We calculated the corresponding correlations $w_1^{\rm gG}$ and $w_2^{\rm gG}$, and their ratio with $R = w_2^{\rm gG}/w_1^{\rm gG}$, following equations (4) and (5) and the description in Section 2.2.

The shear ratio results are shown in Fig. 9. Following the same angular binning as in Fig. 3 for the correlation measurements, we show the shear ratio measurements with different maximum $\theta$ binning. As we include more angular bins at large scale, the constraints on the shear ratio $R$ also improves. Our fiducial analysis uses the two small-scale angular bins with $\theta < \sim 4$ arcmin, since the three large-scale bins are expected in the direct two-point cosmology study, as described in Section 4.1. The current small-scale information can constrain shear ratio at $R = 1.21^{+0.42}_{-0.35}$, as shown in the orange distribution in Fig. 9. The theoretical prediction (using $R = w_2^{\rm gG}/w_1^{\rm gG}$, equations 1 and 3) has a weak angular dependence that varies between 1.13 and 1.18. This small angular variation is due to the angular dependence in $P\left(k = \frac{\ell+1/2}{\chi}, z\right)$ in equation (1), which is not fully cancelled when taking the ratio using correlation functions. We note this weak angular dependence is small and can be easily taken into account in the theoretical predictions.
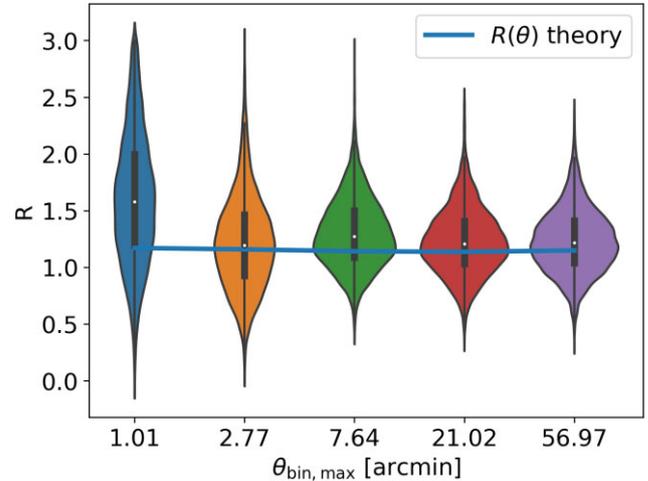


**Figure 9.** The Markov chain Monte Carlo (MCMC) posterior PDF of the shear ratio measurements for BGS×DECaLS using equations (4) and (5), with different maximum $\theta$ binning. The galaxies are distributed as in Fig. 1, with source galaxies split into $0.6 < z_{\rm p} < 0.9$ and $0.9 < z_{\rm p} < 1.5$. The constraint on the shear ratio is stronger when we apply more $\theta$-bins at larger scales. We use the two small-scale angular bins ($\theta < \sim 4$ arcmin, shown in orange) as our fiducial analysis, as in Fig. 3, with a resulting $R = 1.21^{+0.42}_{-0.35}$. All the results agree with the theoretical prediction in the blue $R(\theta)$ curve, which has a weak angular variation between 1.13 and 1.18. When rescaling the covariance to the final overlap of DESI×DECaLS, the shear ratio can be constrained as good as $\sigma_R \sim 0.04$ when using the small-scale information (rescale the orange distribution), and $\sigma_R \sim 0.03$ when using the full scale (rescale the purple distribution).

To predict the constraining power when full DESI finishes, we rescaled the covariance based on the overlapped area as in Table 1, and find the shear ratio can be constrained at $\sigma_R = 0.04$ with the small-scale information, which is not used in getting the $S_8$ constraint. Considering full information for the shear ratio study, we can obtain $\sigma_R = 0.03$. These statistical errors are comparable with the shear ratio studies in Sánchez et al. (2022) with DES-Y3 data, showing a promising future in using shear ratio to improve cosmological constraint and/or to further constrain the systematics (Giblin et al. 2021).

### 4.4 Cosmic magnification

We discussed that the ELG×DECaLS results have low S/N in Figs 6 and 7 and Table 1, as the ELGs are mainly distributed at large-$z$, while the advantage of DECaLS is at low-$z$. On the other hand, this opens a window to the study of cosmic magnification by putting the ELGs at high-$z$ and using shear from low-$z$ DECaLS galaxies. We follow the methodology in Liu et al. (2021) and use galaxy samples distributed as in Fig. 10. The DECaLS galaxies are located at a much lower photo-$z$ compared with the ELGs, as in the targeted shear–magnification correlation, the shear–density correlation exists as a source of systematics when even a small fraction of shear galaxies appear at higher $z$ than the ELGs.

The measurements are shown in Fig. 11. We find positive signals at the small scale, and null detections at the large scale, for all DECaLS, KiDS, and HSC. We tested the $45°$ rotation of the shear, resulting in consistency with 0 on all scales for all the source samples. Considering the similar calculation with the extended Baryon Oscil-
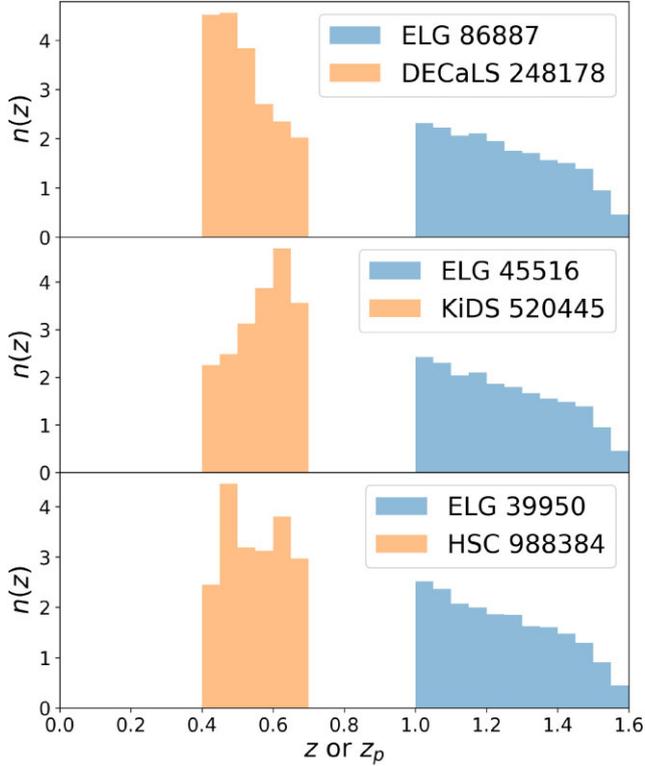
**Figure 10.** The redshift distribution for high-$z$ ELGs ($1 < z < 1.6$) and low-$z$ source galaxies ($0.4 < z_p < 0.7$) for magnification study. The choice of such a large redshift gap is to prevent potential leakage due to photo-$z$ inaccuracy. The numbers in the labels are the number of galaxies in the overlapped region.
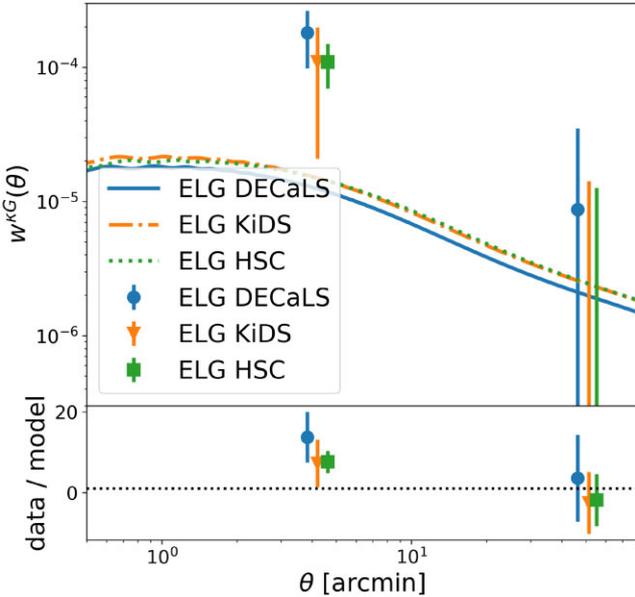


**Figure 11.** The magnification(ELGs)–shear correlation measurements, corresponding to the galaxy samples in Fig. 10. The theoretical curves are based on equation (6), assuming $g_{\mu,\,eff} = 1$ as a reference, and no contribution from intrinsic alignment, which can potential lower the theoretical curve and weaken the measurement. The (small scale, large scale) detection significance for ELG×DECaLS are (2.2, 0.3), for ELG×KiDS are (1.2, −0.3), and for ELG×HSC are (2.8, −0.3). The negative values at the large scale represent negative measurements, which might be due to shot noise, sample variance, or impact from systematics with negative values, like intrinsic alignment if there exists some photo-$z$ outlier.

**Table 2.** Best-fitting amplitude $g_{\mu,\,eff}$ for the cosmic magnification. The upper part corresponds to the results in Fig. 11 for DECaLS, KiDS, HSC, and the combination of them (the 'all' case). We find with the DESI 1 per cent survey, we can already detect cosmic magnification at $\sim 3.1\sigma$ for the shear galaxies distributed at $0.4 < z_p < 0.7$, while the $z_p < 0.4$ galaxies are mainly contributing noise as it corresponding lensing efficiency (equation 2) is low. The degrees of freedom is calculated as dof $= N_{data} - N_{para}$. We see no significant deviation between data and model as $\chi^2/$dof $\sim 1$.

| Case | $g_{\mu,\,eff}$ | S/N | $\chi^2/$dof |
|---|---|---|---|
| DECaLS $0.4 < z_p < 0.7$ | $10.6^{+5.2}_{-5.8}$ | $1.8\sigma$ | 0.6/1 |
| KiDS $0.4 < z_p < 0.7$ | $4.2^{+6.0}_{-5.7}$ | $0.7\sigma$ | 1.3/1 |
| HSC $0.4 < z_p < 0.7$ | $5.6^{+2.3}_{-2.3}$ | $2.4\sigma$ | 1.1/1 |
| All $0.4 < z_p < 0.7$ | $6.1^{+1.9}_{-2.0}$ | $3.1\sigma$ | 3.9/5 |
| All $0 < z_p < 0.7$ | $5.3^{+2.0}_{-2.0}$ | $2.7\sigma$ | 12.5/11 |

lation Spectroscopic Survey (eBOSS) ELGs[4] and DECaLS sources as a reference, we found the measurements are consistent with 0 on all scales, see Appendix B for details. In the measurements of Fig. 11, the null detections at the large scale could be due to cosmic variance or some negative systematics such as intrinsic alignment. The positive measurements at the small scale could be due to the targeted magnification signals, the cosmic variance, or photo-$z$ errors. We note to separate these different signals, either a stronger signal with clear angular dependencies or additional observables are needed to break the degeneracy.

As a further step, we present an effective amplitude fitting of $g_{\mu,\,eff}$ for the magnification signals, following equation (7), in Table 2. We find $\sim 1\sigma$ measurement for KiDS and $\sim 2\sigma$ measurement for DECaLS and HSC. Considering the ELG samples are quite similar as shown in Fig. 10, and the three best-fitting $g_{\mu,\,eff}$ amplitudes are consistent, we evaluated the combined best fit, achieving $\sim 3\sigma$ significance. The covariance between different surveys is ignored for the combined estimation, as shot noise is more dominant in this case than the cosmic variance. Additionally, we find that by including shear galaxies from $0 < z_p < 0.4$, the significance of magnification detection drops, due to the low-$z$ data having much weaker lensing efficiency as in equation (2), and is mainly contributing noise.

The fitting goodness of the reduced $\chi^2$ (defined by the $\chi^2$ between the best fit and the data, divided by the degrees of freedom) is generally close to $\sim 1$ for each case. This shows no significant deviation between the model and the data. The detected $\sim 3\sigma$ positive signal can be either due to the cosmic magnification, or very similar stochastic photo-$z$ outliers between the three lensing surveys. As DECaLS, KiDS, and HSC have totally different photometric bands, photo-$z$ algorithms, and training samples, we think the detected signals are less likely due to the similar photo-$z$ outliers, and more likely to be the cosmic magnification signal. Therefore, by assuming the combined best fit of $g_{\mu,\,eff} \sim 6.1$ as the true value and rescaling the covariance similar to Table 1, we expect $\sim 10\sigma$ detection for DECaLS DR9, which is very promising for a Stage III lensing survey. By then, with a better understanding of the systematics such as IA and photo-$z$ outlier, these cross-correlations can bring very promising constraining power in studying cosmic magnification. We can choose to (1) cut a complete and flux-limited sample and compare it with the flux function; (2) try to use the given DESI completeness and flux function to find a relation of $g_{\mu,\,eff}(\alpha)$ rather than $g_{\mu} = 2(\alpha - 1)$; (3) compare with realistic mocks to infer $g_{\mu,\,eff}$; and (4) add an artificial

[4]https://www.sdss.org/surveys/eboss/

lensing signal $\kappa$ to real data and infer $g_{\mu,\mathrm{eff}}$ as a response $\partial \delta_{\mathrm{g}}^{\mathrm{L}} / \partial \kappa$, similar to metacalibration (Huff & Mandelbaum 2017; Sheldon & Huff 2017) or Fourier Power Function Shapelets (FPFS; Li, Li & Massey 2022b; Li & Mandelbaum 2023).

## 5 CONCLUSIONS

In this work, we study the cross-correlations between DESI 1 per cent survey galaxies and shear measured from DECaLS, one of the imaging surveys for DESI target selection. For the 1 per cent DESI data, DECaLS can have comparable performances compared with the main Stage III lensing surveys KiDS and HSC. More specifically, we measure the cross-correlations of DESI BGS/LRGs/ELGs×different shear catalogue, shown in Figs 2, 5, and 7. We forecast the level of significance with full DESI data in Table 1. Assuming systematic errors can be cleaned with high precision in the future, we find the large-scale S/N could reach $>50\sigma$ for DECaLS×BGS, $>15\sigma$ for DECaLS×LRG, and $>10\sigma$ for DECaLS×ELG, which are very promising before the Stage IV surveys come out.

We point out that the main difficulty in obtaining DECaLS cosmology is the calibrations for the systematics. In order to safely use the large-scale $\sim 50\sigma$ information of BGS×DECaLS, we need to achieve the minimum requirements on (1) the multiplicative bias of $|m| < 0.006$ and (2) the mean of redshift distribution $|\Delta z| < 0.008$, when requiring the introduced bias follows $<0.31\sigma$. To safely use the full-scale $\sim 100\sigma$ data, the requirement is a factor of 2 stronger. The requirement could be even higher when combining different observables, but it will require a larger footprint than the 1 per cent survey for the study. These requirements are essential guides for future calibrations and studies on cosmology.

To fully use the advantage of DECaLS, we further explored two promising observables, the shear ratio and the cosmic magnification. We show the current 1 per cent BGS data can constrain shear ratio with $\sigma_R \sim 0.4$, while the full DESI BGS can give $\sigma_R \sim 0.04$ using only the small-scale information, as shown in Fig. 9. Furthermore, weak detections of potential cosmic magnification are shown in Fig. 11 and Table 2. We discussed how the possible systematics can affect this signal in Section 4.4. We also expect DECaLS to have a strong contribution ($\sim 10\sigma$ detection) to future magnification studies, if the observed signals in this work are not due to fluctuations.

To summarize, DECaLS lensing is a very promising tool that can enrich the cosmological output of DESI. It will bring new cosmological information with its huge footprint. It has great advantages in the large-scale and the low-$z$ information, after carefully addressing the systematics. It will offer strong S/N for shear ratio study, and good potential in measuring cosmic magnification. Careful calibrations of the shear and redshift distribution can result in very promising outcomes.

---

[5] https://github.com/LSSTDESC/CCL (Chisari et al. 2019).
[6] https://github.com/rmjarvis/TreeCorr (Jarvis, Bernstein & Jain 2004).
[7] https://github.com/healpy/healpy (Górski et al. 2005; Zonca et al. 2019).
[8] https://github.com/matplotlib/matplotlib (Hunter 2007).
[9] https://github.com/dfm/emcee (Foreman-Mackey et al. 2013).
[10] https://github.com/dfm/corner.py (Foreman-Mackey 2016).
[11] https://github.com/astropy/astropy (Astropy Collaboration et al. 2013).
[12] https://github.com/pandas-dev/pandas
[13] https://github.com/scipy/scipy (Jones, Oliphant & Peterson 2001).
[14] https://github.com/johannesulf/dsigma

under contract to the U.S. Department of Energy. The complete acknowledgements can be found at https://www.legacysurvey.org/.

The authors are honoured to be permitted to conduct scientific research on Iolkam Du'ag (Kitt Peak), a mountain with particular significance to the Tohono O'odham Nation.

## DATA AVAILABILITY

The data used to produce the figures in this work are available through https://doi.org/10.5281/zenodo.7322710 following DESI Data Management Plan.

## REFERENCES

Abbott T. M. C. et al., 2022, Phys. Rev. D, 105, 023520
Aihara H. et al., 2022, PASJ, 74, 247
Alexander D. M. et al., 2023, AJ, 165, 124
Allende Prieto C. et al., 2020, Res. Notes Am. Astron. Soc., 4, 188
Amon A. et al., 2018, MNRAS, 477, 4285
Amon A. et al., 2022, Phys. Rev. D, 105, 023514
Asgari M. et al., 2021, A&A, 645, A104
Astropy Collaboration et al., 2013, A&A, 558, A33
Bailey S. et al., 2023, in preparation
Begeman K., Belikov A. N., Boxhoorn D. R., Valentijn E. A., 2013, Exp. Astron., 35, 1
Benítez N. et al., 2004, ApJS, 150, 1
Benitez N., 2000, ApJ, 536, 571
Blake C. et al., 2020, A&A, 642, A158
Buchs R. et al., 2019, MNRAS, 489, 820
Chang C. et al., 2019, MNRAS, 482, 3696
Chaussidon E. et al., 2023, ApJ, 944, 107
Chisari N. E. et al., 2019, ApJS, 242, 2
Cooper A. P. et al., 2023, ApJ, 947, 37
de Jong J. T. A. et al., 2015, A&A, 582, A62
Deshpande A. C., Kitching T. D., 2020, Phys. Rev. D, 101, 103531
DESI Collaboration et al., 2023a, preprint (arXiv:2306.06307)
DESI Collaboration et al., 2023b, preprint (arXiv: 2306.06308)
DESI Collaboration et al., 2016a, preprint (arXiv:1611.00036)
DESI Collaboration et al., 2016b, preprint (arXiv:1611.00037)
DESI Collaboration et al., 2022, AJ, 164, 207
Dey A. et al., 2019, AJ, 157, 168
Dong F., Zhang P., Sun Z., Park C., 2022, ApJ, 938, 72
Duffy A. R., Schaye J., Kay S. T., Dalla Vecchia C., 2008, MNRAS, 390, L64
Duncan K. J., 2022, MNRAS, 512, 3662
Erben T. et al., 2013, MNRAS, 433, 2545
Euclid Collaboration et al., 2019, A&A, 627, A59
Favole G. et al., 2016, MNRAS, 461, 3421
Fenech Conti I., Herbonnet R., Hoekstra H., Merten J., Miller L., Viola M., 2017, MNRAS, 467, 1627
Fong M., Choi M., Catlett V., Lee B., Peel A., Bowyer R., King L. J., McCarthy I. G., 2019, MNRAS, 488, 3340
Fong M., Han J., 2021, MNRAS, 503, 4250
Foreman-Mackey D., 2016, J. Open Source Softw., 1, 24
Foreman-Mackey D., Hogg D. W., Lang D., Goodman J., 2013, PASP, 125, 306
Gao H., Jing Y. P., Zheng Y., Xu K., 2022, ApJ, 928, 10
Giblin B. et al., 2021, A&A, 645, A105
Gong Y. et al., 2019, ApJ, 883, 203
Gonzalez-Nuevo J., Cueli M. M., Bonavera L., Lapi A., Migliaccio M., Argüeso F., Toffolatti L., 2021, A&A, 646, A152
Górski K. M., Hivon E., Banday A. J., Wandelt B. D., Hansen F. K., Reinecke M., Bartelmann M., 2005, ApJ, 622, 759
Guy J. et al., 2023, AJ, 165, 43
Hahn C. et al., 2023, AJ, 165, 253
Hamana T. et al., 2020, PASJ, 72, 16

Harnois-Déraps J., Martinet N., Castro T., Dolag K., Giblin B., Heymans C., Hildebrandt H., Xia Q., 2021, MNRAS, 506, 1623
Hartlap J., Simon P., Schneider P., 2007, A&A, 464, 399
Heymans C. et al., 2012, MNRAS, 427, 146
Heymans C. et al., 2021, A&A, 646, A140
Hikage C. et al., 2019, PASJ, 71, 43
Hildebrandt H. et al., 2017, MNRAS, 465, 1454
Huff E., Mandelbaum R., 2017, preprint (arXiv:1702.02600)
Hunter J. D., 2007, Comput. Sci. Eng., 9, 90
Jarvis M. et al., 2016, MNRAS, 460, 2245
Jarvis M., Bernstein G., Jain B., 2004, MNRAS, 352, 338
Jedamzik K., Pogosian L., Zhao G.-B., 2021, Commun. Phys., 4, 123
Joachimi B. et al., 2021, A&A, 646, A129
Jones E., Oliphant T., Peterson P. , 2001, SciPy: Open Source Scientific Tools for Python. http://www.scipy.org/
Joudaki S. et al., 2018, MNRAS, 474, 4894
Jullo E. et al., 2019, A&A, 627, A137
Kannawadi A. et al., 2019, A&A, 624, A92
Kitanidis E., White M., 2021, MNRAS, 501, 6181
Kong H. et al., 2020, MNRAS, 499, 3943
Lan T.-W. et al., 2023, ApJ, 943, 68
Lang D., Hogg D. W., Schlegel D. J., 2016, AJ, 151, 36
Laureijs R. et al., 2011, preprint (arXiv:1110.3193)
Leauthaud A. et al., 2017, MNRAS, 467, 3024
Leauthaud A. et al., 2022, MNRAS, 510, 6150
Lee S. et al., 2022, MNRAS, 509, 2033
Levi M. et al., 2013, preprint (arXiv:1308.0847)
Li H., Zhang J., Liu D., Luo W., Zhang J., Dong F., Shen Z., Wang H., 2021, ApJ, 908, 93
Li X. et al., 2022a, PASJ, 74, 421
Li X. et al., 2023, preprint (arXiv:2304.00702)
Li X., Li Y., Massey R., 2022b, MNRAS, 511, 4850
Li X., Mandelbaum R., 2023, MNRAS, 521, 4904
Lin W., Ishak M., 2017, Phys. Rev. D, 96, 083532
Liu X., Liu D., Gao Z., Wei C., Li G., Fu L., Futamase T., Fan Z., 2021, Phys. Rev. D, 103, 123504
LSST Science Collaboration et al., 2009, preprint (arXiv:0912.0201)
Mandelbaum R. et al., 2005, MNRAS, 361, 1287
Mandelbaum R. et al., 2015, MNRAS, 450, 2963
Mandelbaum R. et al., 2018, PASJ, 70, S25
Mandelbaum R., 2018, ARA&A, 56, 393
Mandelbaum R., Hirata C. M., Ishak M., Seljak U., Brinkmann J., 2006, MNRAS, 367, 611
Massey R. et al., 2013, MNRAS, 429, 661
Mead A. J., Brieden S., Tröster T., Heymans C., 2021, MNRAS, 502, 1401
Meisner A. M., Lang D., Schlegel D. J., 2017, AJ, 154, 161
Miller L. et al., 2013, MNRAS, 429, 2858
Miller T. et al., 2023, preprint (arXiv: 2306.06310)
Moustakas J. et al., 2023, preprint (arXiv: 2307.04888)
Myers A. D. et al., 2023, AJ, 165, 50
Navarro J. F., Frenk C. S., White S. D. M., 1996, ApJ, 462, 563
Niemiec A. et al., 2017, MNRAS, 471, 1153
Peng H., Xu H., Zhang L., Chen Z., Yu Y., 2022, MNRAS, 516, 6210
Perivolaropoulos L., Skara F., 2022, New Astron. Rev., 95, 101659
Phriksee A., Jullo E., Limousin M., Shan H., Finoguenov A., Komonjinda S., Wannawichian S., Sawangwit U., 2020, MNRAS, 491, 1643
Planck Collaboration I, 2020, A&A, 641, A1
Prat J. et al., 2022, Phys. Rev. D, 105, 083528
Pujol A., Bobin J., Sureau F., Guinot A., Kilbinger M., 2020, A&A, 643, A158
Raichoor A. et al., 2020, Res. Notes Am. Astron. Soc., 4, 180
Raichoor A. et al., 2023, AJ, 165, 25
Refregier A., 2003, ARA&A, 41, 645
Ruiz-Macias O. et al., 2020, Res. Notes Am. Astron. Soc., 4, 187
Sánchez C. et al., 2022, Phys. Rev. D, 105, 083529
Schlafly E. et al., 2023, preprint (arXiv: 2306.06309)
Schlegel D. et al., 2023, preprint (arXiv: 2209.03585)
Secco L. F. et al., 2022, Phys. Rev. D, 105, 023515

Shan H. et al., 2018, MNRAS, 474, 1116

Sheldon E. S., Becker M. R., MacCrann N., Jarvis M., 2020, ApJ, 902, 138

Sheldon E. S., Huff E. M., 2017, ApJ, 841, 24

Silber J. H. et al., 2023, AJ, 165, 9

Spergel D. et al., 2015, preprint (arXiv:1503.03757)

Sun Z., Zhang P., Dong F., Yao J., Shan H., Jullo E., Kneib J.-P., Yin B., 2023, ApJS, 267, 21

Takada M., Hu W., 2013, Phys. Rev. D, 87, 123504

Takada M., Jain B., 2004, MNRAS, 348, 897

Takahashi R., Sato M., Nishimichi T., Taruya A., Oguri M., 2012, ApJ, 761, 152

Tanaka M. et al., 2018, PASJ, 70, S9

Tinker J. L., Robertson B. E., Kravtsov A. V., Klypin A., Warren M. S., Yepes G., Gottlöber S., 2010, ApJ, 724, 878

Tinker J., Kravtsov A. V., Klypin A., Abazajian K., Warren M., Yepes G., Gottlöber S., Holz D. E., 2008, ApJ, 688, 709

van den Busch J. L. et al., 2020, A&A, 642, A200

von Wietersheim-Kramsta M. et al., 2021, MNRAS, 504, 1452

Wang Y. et al., 2020, MNRAS, 498, 3470

Wright A. H. et al., 2019, A&A, 632, A34

Wright A. H., Hildebrandt H., van den Busch J. L., Heymans C., 2020, A&A, 637, A100

Wright E. L. et al., 2010, AJ, 140, 1868

Xu W. et al., 2021, ApJ, 922, 162

Yamamoto M., Troxel M. A., Jarvis M., Mandelbaum R., Hirata C., Long H., Choi A., Zhang T., 2023, MNRAS, 519, 4241

Yang X., Zhang J., Yu Y., Zhang P., 2017, ApJ, 845, 174

Yao J. et al., 2023, preprint (arXiv:2304.04489)

Yao J., Ishak M., Lin W., Troxel M. A., 2017, J. Cosmol. Astropart. Phys., 10, 056

Yao J., Shan H., Zhang P., Kneib J.-P., Jullo E., 2020, ApJ, 904, 135

Yèche C. et al., 2020, Res. Notes Am. Astron. Soc., 4, 179

Zhang P., 2010, ApJ, 720, 1090

Zhang P., Liguori M., Bean R., Dodelson S., 2007, Phys. Rev. Lett., 99, 141302

Zhang P., Pen U.-L., Bernstein G., 2010, MNRAS, 405, 359

Zhou R. et al., 2020, Res. Notes Am. Astron. Soc., 4, 181

Zhou R. et al., 2021, MNRAS, 501, 3309

Zhou R. et al., 2023, AJ, 165, 58

Zonca A., Singer L., Lenz D., Reinecke M., Rosset C., Hivon E., Gorski K., 2019, J. Open Source Softw., 4, 1298

Zou H. et al., 2017, PASP, 129, 064101

Zou H., Gao J., Zhou X., Kong X., 2019, ApJS, 242, 8

Zu Y. et al., 2021, MNRAS, 505, 5117

## APPENDIX A: THEORETICAL COVARIANCE

In this appendix, we test the Gaussian covariance assumption being used in Table 1. We use DECaLS×BGS and KiDS×BGS as examples, using the same galaxy number densities and redshift distributions as in Fig. 1, and the same area as shown in Table 1. The angular power spectrum $C^{gG}(\ell)$ is calculated within range $10 < \ell < 10\,000$, binned with $\Delta\ell = 0.2\ell$, thus total 37 angular bins. We follow the procedures in Joachimi et al. (2021) and divide the components into Gaussian covariance, connected non-Gaussian covariance, and supersample covariance.

The Gaussian covariance is calculated by

$$\mathrm{Cov_G}(\ell_1, \ell_2) = \frac{\delta_{\ell_1,\ell_2}}{(2\ell+1)\Delta\ell f_{sky}} \left[ \left(C^{gG}\right)^2 + \left(C^{gg} + N^{gg}\right)\left(C^{GG} + N^{GG}\right) \right], \text{(A1)}$$

where $\delta_{\ell_1,\ell_2}$ is the Kronecker delta function; $C^{gG}$, $C^{gg}$, and $C^{GG}$ are the galaxy–lensing, galaxy–galaxy, lensing–lensing angular power spectrum, respectively; $N^{gg} = 4\pi f_{sky}/N_g$ and $N^{GG} = 4\pi f_{sky}\gamma^2_{rms}/N_G$ are the shot noise for $C^{gg}$ and $C^{GG}$, where $f_{sky}$ is the fraction of sky of the overlapped area, $N_g$ and $N_G$ are the total number of the galaxies for the lens and source.
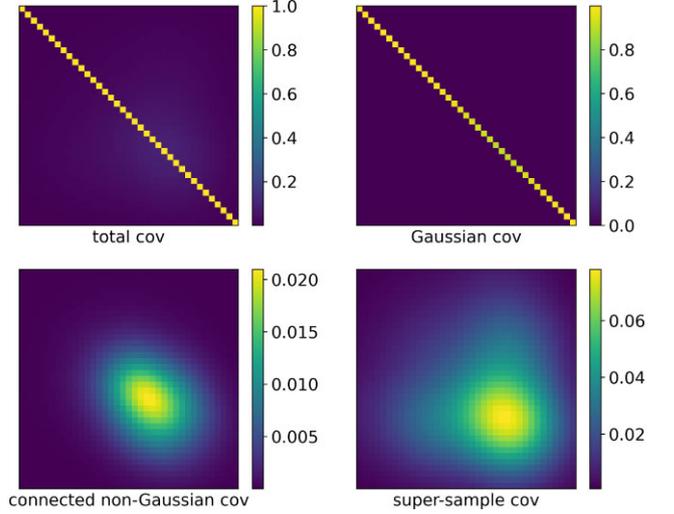


**Figure A1.** The theoretical covariance matrix (normalized, i.e. correlation coefficient) for the DECaLS×BGS angular power spectrum, corresponding to the measurements in Fig. 3 and the DECaLS results in Fig. 2. It is clear that the Gaussian component in the total covariance is much larger than the connected non-Gaussian component and the supersample covariance component.

The connected non-Gaussian covariance (Takada & Jain 2004) is calculated by

$$\mathrm{Cov_{cNG}}(\ell_1, \ell_2) = \int \mathrm{d}\chi \frac{b_g^2 n_l^2(\chi) q_s^2(\chi)}{\chi^6} T_m\left(\frac{\ell_1 + 1/2}{\chi}, \frac{\ell_2 + 1/2}{\chi}, a(\chi)\right), \text{(A2)}$$

where $n_l$ and $q_s$ are the lens distribution and source lensing efficiency, $b_g$ denotes the lens galaxy bias, $\chi$ denotes the comoving distance, same as those in equation (1); $T_m$ is the matter trispectrum, calculated using a halo model formalism (Joachimi et al. 2021). We assume the Navarro–Frenk–White (NFW) halo profile (Navarro, Frenk & White 1996) with a concentration–mass relation (Duffy et al. 2008), a halo mass function (Tinker et al. 2008), and a halo bias (Tinker et al. 2010).

The supersample covariance (Takada & Hu 2013) is calculated by

$$\mathrm{Cov_{SSC}}(\ell_1, \ell_2) = \int \mathrm{d}\chi \frac{b_g^2 n_l^2(\chi) q_s^2(\chi)}{\chi^6} \frac{\partial P_\delta(\ell_1/\chi)}{\partial\delta_b} \frac{\partial P_\delta(\ell_2/\chi)}{\partial\delta_b} \sigma_b^2(\chi), \text{(A3)}$$

where the derivative of $\partial P_\delta/\partial\delta_b$ gives the response of the matter power spectrum to a change of the background density contrast $\delta_b$, while $\sigma_b^2$ denotes the variance of the background matter fluctuations in the given footprint. In this test, we use a circular disc that covers the same area as the given survey to calculate $\sigma_b^2$.

The calculation is performed with the halo model tools in PYCCL. We show the results of DECaLS×BGS in Fig. A1 and KiDS×BGS in Fig. A2. It is clear that the contribution from connected non-Gaussian covariance and supersample covariance in DECaLS is negligible, so a Gaussian covariance can be fairly assumed for DECaLS in Table 1. The Gaussian covariance is still dominant in KiDS, however, the contribution from the other two is not negligible. Therefore, due to the small footprint, the forecasted S/N for KiDS and HSC in Table 1 no longer scales exactly with the overlapped area.

We note that this test for different components of the covariance is only used to make an estimated comparison. Before using those covariances directly in the study, one needs to take care of the non-linear galaxy bias $b_g$, the exact shape of the footprint that produces $\sigma_b^2$, and build simulations to validate the accuracy of the theoretical covariance transferring from angular power spectrum to correlation functions as in Joachimi et al. (2021). Therefore, we choose to stick
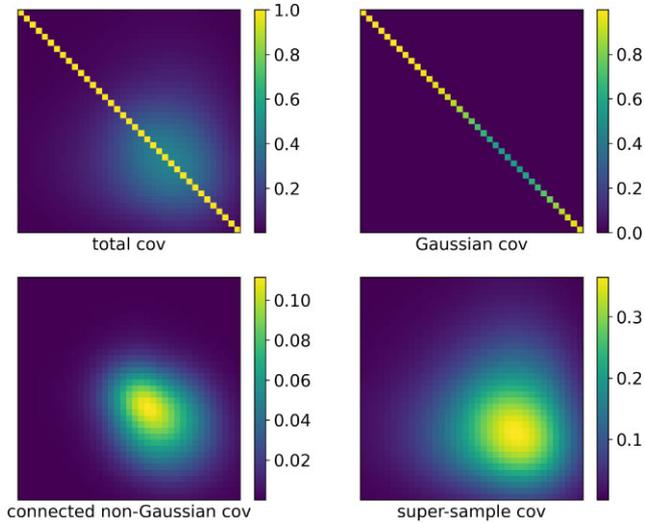
**Figure A2.** The theoretical covariance matrix (normalized, i.e. correlation coefficient) for the KiDS×BGS angular power spectrum, corresponding to the measurements of the KiDS results in Fig. 2. The Gaussian component in the total covariance is still the dominant part. But the connected non-Gaussian component and the supersample covariance component are relatively larger than Fig. A1 and are no longer negligible.

with the data-driven jackknife covariance introduced in the main text, while we note that this effect could potentially reduce the forecasted S/N for KiDS and HSC in Table 1.

## APPENDIX B: EBOSS ELGS×DECALS SHEAR

We show the cosmic magnification measurements using eBOSS ELGs×DECaLS shear, following a similar procedure as described in Sections 2.3 and 4.4. The overlapped area between eBOSS ELGs and DECaLS shear is ∼930 deg², which enables us to use 200 jackknife subregions and five angular bins, while we calculate the correlation in the angular range of $0.5 < \theta < 120$ arcmin, which is wider than Fig. 3, see discussions in Section 4.1.

In Fig. B1, we show the galaxy redshift distribution being used in this measurement. We see that the eBOSS ELGs are distributed at lower redshift compared with DESI ELGs in Fig. 10, and more galaxies are used in this eBOSS measurement. The corresponding correlation function measurement is shown in Fig. B2, which is consistent with 0. We think this is due to the fact that the galaxy number density for the eBOSS ELGs is much lower than the DESI ELGs, leading to a larger shot noise.
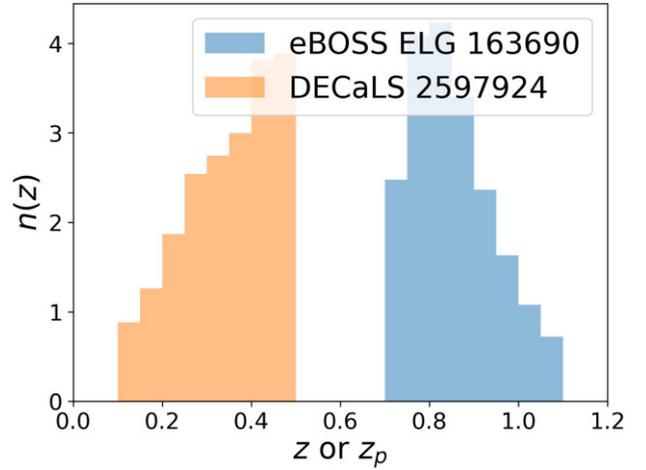


**Figure B1.** The galaxy redshift distribution for the eBOSS ELGs (blue) and photo-$z$ distribution for DECaLS (orange). We use $0 < z_{\rm p} < 0.5$ for DECaLS and $z > 0.7$ for eBOSS ELGs. The redshift ranges are generally lower than in Fig. 10 as eBOSS ELGs are at lower redshift than DESI ELGs.
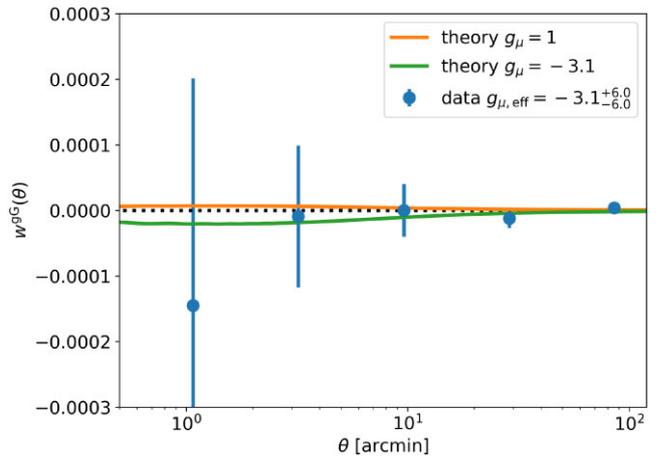


**Figure B2.** The magnification(ELGs)–shear correlation measurements for eBOSS×DECaLS. Unlike Fig. 11 for DESI, this measurement is consistent with 0.

This paper has been typeset from a TeX/LaTeX file prepared by the author.